Chinese Journal of Aeronautics, 2013,**26**(2): 269–278

Chinese Society of Aeronautics and Astronautics
& Beihang University

**Chinese Journal of Aeronautics**

cja@buaa.edu.cn
www.sciencedirect.com

# Plume aerodynamic effects of cushion engine in lunar landing

**He Bijiao, He Xiaoying, Zhang Mingxing, Cai Guobiao** *

*School of Astronautics, Beihang University, Beijing 100191, China*

Received 26 October 2011; revised 19 December 2011; accepted 2 May 2012
Available online 6 March 2013

**KEYWORDS**

Boundary blocks;
Cushion engines;
Lunar landing;
Monte Carlo methods;
Plume effects

**Abstract** During the second period of China "Tanyue" Project, the explorer will softland on the moon. The cushion engines are used to decelerate the explorer and reduce the impact on the lunar ground. It is necessary to study its plume effects on the explorer component. The self-developed PWS (Plume WorkStation) software based on direct simulation Monte Carlo (DSMC) method is used to simulate the plume effects of two 150 N engines. Due to the complex structure of the explorer, PWS uses a decoupling method to treat the boundary mesh, which mainly interacts with simulation particles, and has no relation with the computational grids. After the analytical expressions of plane surfaces and curved surfaces of each boundary block are given, the particle position within or without the boundary blocks can be easily determined. Finally the 3D plume field of two 150 N engines is simulated. The pressure, temperature and velocity distributions of plume field are clearly presented by three characteristic slices. The aerodynamic effects on the explorer bottom, the landfall legs and antenna are separately shown. The compression influence on the plume flow of four landfall legs can be observed.



## 1. Introduction

Moon exploration is one of the most important objectives of Chinese astronautics career. According to the known facts the environment of lunar surface is highly vacuum, nonmagnetic, low gravitational, and clean. It is an ideal location for earth observation and deep space exploration. During the second period of China "Tanyue" Project, the explorer would softland on the moon with the help of cushion engines. The cushion engines are used to decelerate the explorer and reduce the impact on the lunar ground. Three types of engines are applied: twelve 10 N thrusters, twelve 150 N thrusters and one variational thruster, of which the thrust can varies from 1500 N to 7500 N.

Due to the complex structure of explorer and large number of engines, it is necessary to consider the engine plume effects on the other equipments loaded on the explorer. The effects mainly consist of two parts: the aerodynamic force and thermal influence of engine plume. The aerodynamic force may exert a disturbance torque on the explorer centroid, which can be large enough to result in the explorer reversal. The aerodynamic thermal load may heat the solar battery and sensors and induce the wrong readings and degrade their performance.

* Corresponding author. Tel.: +86 10 82336533.
E-mail address: cgb@buaa.edu.cn (G. Cai).

Peer review under responsibility of Editorial Committe of CJA.

Production and hosting by Elsevier

1000-9361 © 2013 Production and hosting by Elsevier Ltd. on behalf of CSAA & BUAA. Open access under CC BY-NC-ND license.
http://dx.doi.org/10.1016/j.cja.2013.02.003

The direct simulation Monte Carlo (DSMC) method, developed by Bird is usually utilized to numerically simulate the rarefied plume field.[1] In the several decades many simulation software based on DSMC method are proposed, such as DAC (DSMC Analysis Code) developed by LeBeau in Johnson Space Center,[2–4] SMILE (Statistical Modeling In Low-density Environment) by Ivanov in the Institute of Theoretical and Applied Mechanics of Russia,[5–10] and MONACO by Boyd of Cornell University.[11–15]

DAC and SMILE employ the structured grid boundary element, while MONACO employs the unstructured triangular grid boundary element. Because this kind of boundary structures is related closely with computation grids, the information of the boundary surfaces should be distributed to the nodes of every grid. Therefore a large amount of storage memory is needed. The main shortcoming is that the computation grids should be quite restricted to the boundary shapes, while the shape is quite complex. Actually the DSMC method requires that the mesh size should be chosen according to the number of local gas molecules. While the boundary surface gets more complex, it grows more difficult to decide the mesh grid near the boundary.

The PWS (Plume WorkStation) software is proposed, which is developed by the research team of Beihang University, China.[16–18] It employs a decoupling method treat the boundary mesh. The boundary borders mainly interact with particles, and have no relation with the computational grids. It uses a two-level construction method to achieve the universality of the boundary conditions. The plume force and thermal effects on the explorer components in lunar landing are simulated using the PWS, involving two 150 N cushion engines working.

## 2. DSMC method and PWS software

The DSMC method is a direct simulation method for rarefied gas dynamics, which is based on the hypothesis of dilute gas. A large number of simulation particles are used to represent the large number of gas molecules in the actual flows. All particles have parameters of position, velocity, diameter and internal energy. Particles move and collide in every time step and the flow field parameters are finally statistically obtained based on the contribution of all the simulation particles.

PWS, a plume calculating software based on DSMC, has six main function modules: particle module (for storage of particle parameters), grid module, particle entry module, particle motion module, boundary module and particle collision module. To improve the calculation speed, a parallel module is also applied. The construction chart and communication among the modules are shown in Fig. 1.

The software is universal, modularized and object-oriented. Every module has various options. The rectangular grid can be set as either equidistant or geometric. The kind of gas molecules can be larger than one. The collision models of gas molecules contain HS (Hard Sphere), VHS (Variable Hard Sphere) and VSS (Variable Soft Sphere). The internal energy is distributed by Larsen-Borgnakke method with consideration of vibrational and rotational freedom degree. The interaction model of gas molecules and solid wall can be chosen as specular reflection, diffuse reflection, Maxwell refection or CLL (Cercignani-Lampis-Lord) reflection models. The boundary condition can be combined by different shaped blocks with different reflection models. The parallel computation can be continued based on the results in store.

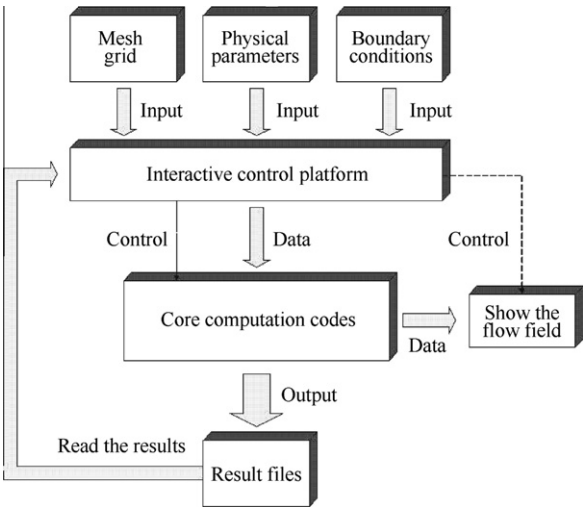


**Fig. 1** Construction chart and communication among the modules in PWS software.

The complex combination of boundary blocks can be realized by using a two-level construction. All the complex surfaces of actual objects are found to be made up of simple surfaces or lines. These simple surfaces can then be divided into linear surface and quadratic surface. In numerical simulation, the structure of objects can be simplified and constructed with linear surface and quadratic surface.

For a 3D object, the construction function can be written as:

$$\begin{cases} a_{1i}x + b_{1i}y + c_{1i}z + d_{1i} \leqslant 0, \quad i = 1, 2, \cdots, n_1 \\ \mathrm{aa}_{2j}x^2 + \mathrm{bb}_{2j}y^2 + \mathrm{cc}_{2j}z^2 + \mathrm{ab}_{2j}xy + \mathrm{bc}_{2j}yz + \mathrm{ca}_{2j}zx \\ \quad + a_{2i}x + b_{2i}y + c_{2i}z + d_{2i} \leqslant 0, \quad j = 1, 2, \cdots, n_2 \end{cases} \tag{1}$$

where $x$, $y$, $z$ are the coordinate values; $a$, $b$, $c$, $d$, aa, bb, cc, ab, bc, ca are the function coefficients; the subscript $i$ means the $i$th linear function; the subscript $j$ means the $j$th quadratic function; $n_1$ means the total number of linear functions; $n_2$ means the total number of quadratic functions; the subscript 1 and 2, respectively note the coefficients for linear and quadratic functions.

Usually the complex bodies can be divided into several simple convex bodies. Generation process for boundary conditions is as follows: (1) at first several often-used plane surfaces and curved surfaces are defined as basic elements; (2) then a convex body can be constituted with these simple plane surfaces or curved surfaces by using the "and" operator; (3) finally the complex object is obtained with several convex bodies by using the "or" operator.

In this way, the solid borders could be treated as combination of several basic types. Because the analytical expressions of plane surfaces and curved surfaces are obviously given, the particle position within or without the boundary blocks can be easily determined. Due to the decoupling character of boundary mesh and flow field mesh, the boundary block grid can be set at arbitrary sizes as the user likes.

The following shows an example of boundary construction. A cylinder is located on a plat surface. The expression for the

plane (Block 1) is $a_{11}x + b_{11}y + c_{11}z + d_{11} \leqslant 0$. The expressions for the side and underside of the cylinder (Block 2) are $a_{21}R + c_{21}z + d_{21} \leqslant 0$ and $a_{12}x + b_{12}y + c_{12}z + d_{12} \leqslant 0$, where $R = \sqrt{x^2 + y^2}$ is the radius of the cylinder. The aggregate of Block 1 and Block 2 forms the given boundary body as shown in Fig. 2.

Because the cylinder goes through the plat surface, some grids of plat fall in the cylinder interior, which makes the efficient area of flat decrease. The modification method should be added to ensure the right interaction of gas molecules on the surface. At first a certain number of random points on the plat surface are generated. Then their positions are judged whether in or out of other blocks. The points beyond any other block are labeled as efficient points. The ratio of the efficient point number to the total point number is labeled as area modification coefficient. The modified grid area (see Fig. 4) is obtained by multiplying the original area (see Fig. 3) with the coefficient. The new center point of mesh grid can be averaged by all the effective points (see Fig. 5).

## 3. Verification

With the improved functions as described above, it is easy for PWS to construct a numerical simulation platform based on

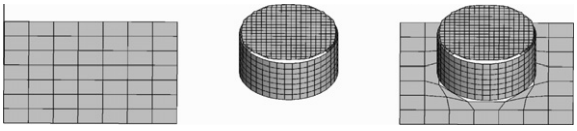

**Fig. 2** Generation of Block 1 and Block 2.

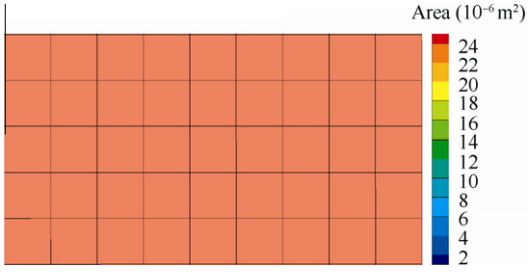


**Fig. 3** Original mesh area of Block 1.

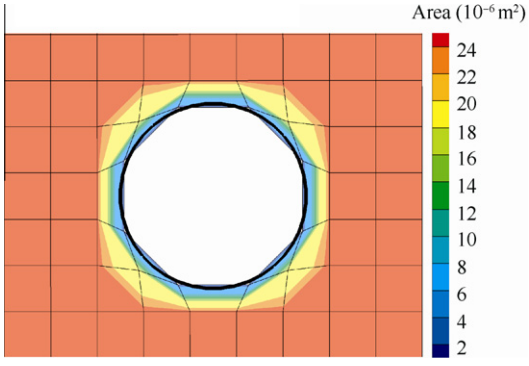


**Fig. 4** Modified mesh area of Block 1.

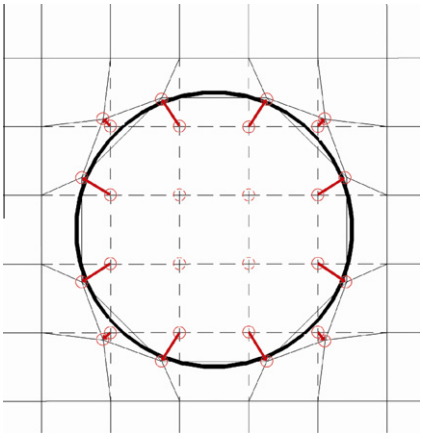

**Fig. 5** Sketch of center point offset in modified mesh.

various actual problems. Two test cases are conducted to verify the particle collision and the interaction model of gas molecule and solid surface.

### 3.1. Particle collision

The experimental data of the seventh commissioning performed by Holden[19] in Calspan-University at Buffalo Research Center (CUBRC), are used as the correlating data. CUBRC is an experiment designed to measure the aerodynamic force and aerodynamic heat flow of a supersonic rarefied flow on a double cone. The shape of the double cone used in the experiment is shown in Fig. 6. Fig. 7 shows the grid geometry of the double cone in the numerical simulation. The coming gas is chosen as $N_2$, with a density of $1.757 \times 10^{-4}$ kg/m$^3$, a temperature of 42.6 K, a pressure of 2.23 Pa, and a velocity of 2073 m/s. The temperature of cone surface is 297.2 K. According to the gas parameters the gas molecule free path can be obtained as 0.42 mm.

The DSMC computation region is 0.2 m × 0.15 m with mesh grid of 1000 × 750. The grid size is 0.2 mm × 0.2 mm. The parallel computation is conducted on a cluster of 64 CPU. The total time cost is about 34.8 h. The number of

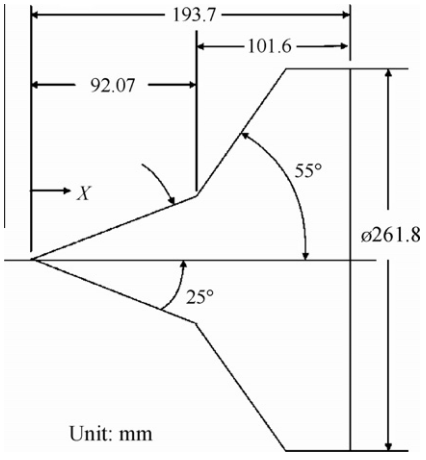


**Fig. 6** Configuration of the double cone in the "CUBRC" experiment.

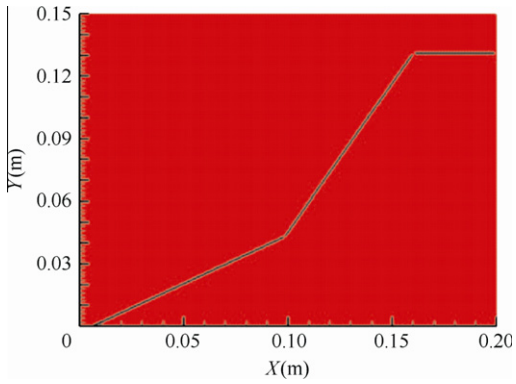


**Fig. 7** Grid geometry of the double cone in numerical simulation.

particles used in simulation is $1.3 \times 10^8$. A comparison test case is also computed to understand the effect of mesh grid. It is labeled as $DSMC_{low}$, in which the mesh grid of $400 \times 300$. The grid size is 0.5 mm × 0.5 mm.

Fig. 8 shows the comparison between the CUBRC data and the calculated results with PWS about the pressure on the double cone surfaces. Fig. 9 shows the comparison between the CUBRC data and the calculated results with PWS about the heat flow on the double cone surfaces. In the two figures, $p_{s\_c}$ is the pressure on the surface of the double cone (Pa); $q_{s\_c}$ is the heat flow on the surface of the double cone ($W/m^2$); $x$ is the coordinate value (m) of the calculating point in the projection of the centerline, and the origin is the summit of the double cone.

As can be seen from Figs. 8 and 9, the values of pressure and heat flow generated with PWS are identical with the CUBRC results, with the maximum or minimum values more or less the same. Except for two points, the deviation of pressure between the calculated values and the CUBRC experimental results at other points is in the range of ±20% and the deviation of heat flow between them is between −30% and +10%, especially at the joints of the double cone. By comparing the results with experimental values, PWS is proved to be highly reliable.

The aerodynamic force results obtained at grid size of 0.2 mm ($\lambda/3$–$2\lambda/3$, where $\lambda$ is the molecular mean free path)

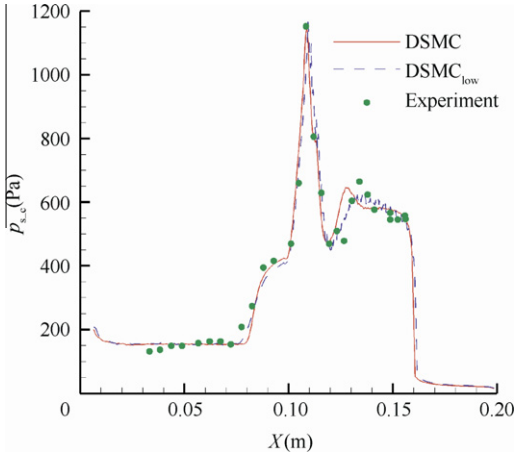


**Fig. 8** Comparison of the CUBRC data and the PWS solutions about the pressure on the double cone surface.

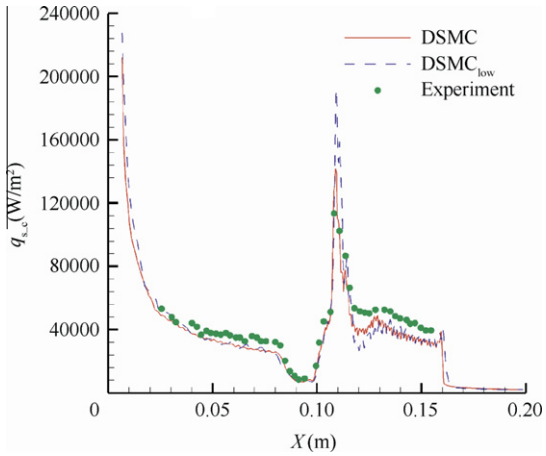


**Fig. 9** Comparison of the CUBRC data and the PWS solutions about the heat flux density on the double cone surface.

agree well with that of 0.5 mm ($> \lambda$). The heat flow results in two cases generally follow the same trend. Only the maximum value differs at some positions, and the peak value of heat flux is higher with the bigger grid size.

### 3.2. Gas-surface interaction

The air at the altitude of 350 km is quite rarefied, and the atmosphere flow is free molecular. The aerodynamic effect of free molecular flow on the simple-shaped objects can be given by the theoretical solutions.[1] The expression of aerodynamic force on the spherical surface is as follows:

$$F = \frac{1}{2}\rho U^2 \pi r^2 \times \left[\frac{e^{-S^2}}{\sqrt{\pi}S^3}(1+2S^2) + \frac{4S^4+4S^2-1}{2S^4}\mathrm{erf}(S) + \frac{2\sigma\sqrt{\pi}}{3S_w}\right] \quad (2)$$

where $\rho$ is the gas density, $U$ the gas velocity, $r$ the sphere radius, $\sigma$ the thermal accommodation coefficient of gas-surface interaction; $S = U/\sqrt{2RT}$, is the gas speed ratio, $R$ the gas constant, $T$ the gas temperature; $S_w$ represents the gas speed ratio on the solid surface; erf(·) is the error function.

The expression of aerodynamic force on the vertical surface is as follows:

$$F = \frac{1}{2}\rho U^2 A \times \left[\left(\frac{2e^{-S^2}}{\sqrt{\pi}S} + \frac{2S^2+1}{S^2}\mathrm{erf}(S)\right)(2-\sigma) + \frac{\sigma\sqrt{\pi}}{S_w}\right] \quad (3)$$

where $A$ is the surface area.

The component ratio of air is given by the NRLMSISE00 atmosphere mode, and the gas constant is computed to be 451.85 $m^2/(s^2 \cdot K)$. The sphere diameter is set as 1.5 m, and air gas velocity is 7800 m/s. $\sigma$ is chosen to be 1.0. The computation region and mesh grid are shown in Fig. 10. Local mesh refinement can be seen near the sphere.

The density of plume field is shown in Fig. 11.

Another case is computed by displacing the sphere with a cylinder. The density of plume field is shown in Fig. 12.

As shown in Table 1, the aerodynamic force is computed in this simulation. By comparing to the theoretical value, the relative error is about 1.2%. Relative error is computed as:

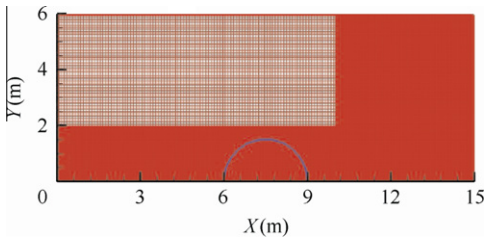


**Fig. 10** Computation region and mesh grid for sphere case.

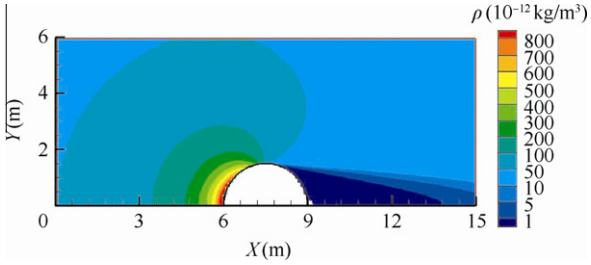


**Fig. 11** Density contours of plume field for sphere case.

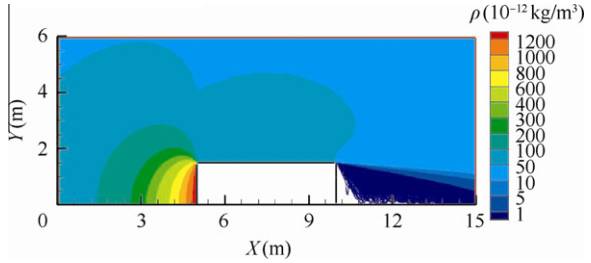


**Fig. 12** Density contours of plume field for cylinder case.

**Table 1** Results of two test cases.

| Case | Simulation value | Theoretical value | Relative error/% |
|---|---|---|---|
| Sphere | 0.021233 | 0.021493 | −1.2 |
| Cylinder | 0.021491 | 0.021753 | −1.2 |

(simulation value − theoretical value)/theoretical value. The results express that the computation model of interaction of gas molecule and solid surface is feasible and precise.

## 4. Simulation

### *4.1. Calculation conditions*

The diameters of nozzle throat and exit of 150 N engine are 11.7 mm and 117 mm. The nozzle exhaust expands directly into the vacuum. The gas parameters at the exit plane are computed by solving Navier-Stokes equations. Then DSMC method is used to calculate the outside plume field. The nozzle exit plane is used as the particle entry section for DSMC simulation. $N_2$, $H_2O$, $H_2$, $CO_2$ and CO are chosen as stimulant molecules, and the mass ratios are given in Table 2.

**Table 2** Mass ratio of main combustion products for 150 N thruster.

| Index | Species | Mass ratio |
|---|---|---|
| 1 | $N_2$ | 0.4181 |
| 2 | $H_2O$ | 0.2968 |
| 3 | $H_2$ | 0.0147 |
| 4 | $CO_2$ | 0.0931 |
| 5 | CO | 0.1704 |

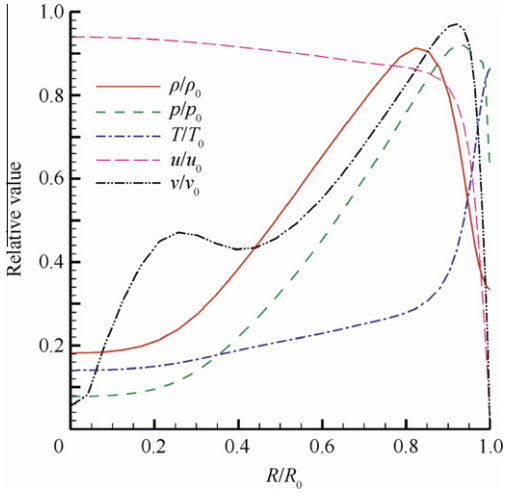


**Fig. 13** Distribution of gas parameters at nozzle exit.

The normalized gas parameters at the nozzle exit are shown in Fig. 13. The normalization parameters are chosen as follows: the gas density $\rho_0 = 0.0025$ kg/m$^3$; the gas pressure $p_0 = 1000$ Pa; the gas temperature $T_0 = 3000$ K; the axial gas velocity $u_0 = 3500$ m/s; the radial gas velocity $v_0 = 400$ m/s; the radial distance from the nozzle exit along the central axis $R_0 = 0.058$ m.

Fig. 14 is the distribution of gas Knudsen number *Kn*. The characteristic length is computed as follows: $L = \rho/(\mathrm{d}\rho/\mathrm{d}x)$. It can be observed that the maximum value is no larger than 0.015. So the exhaust flow falls into continuum flow region. It is reasonable to choose the exit plane as the interface of Navier-Stokes solution and DSMC method.

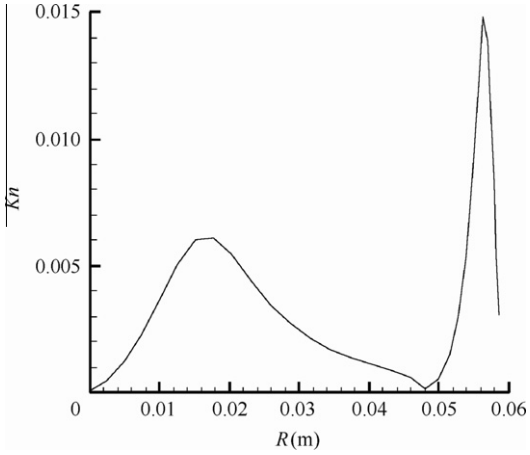


**Fig. 14** Gas Knudsen number distribution.

The computation region of flow field is a complex 3D model. To reduce the large computation cost only 1/4 of the flow region is computed due to the structure symmetry. The computation region is set as 2 m × 2 m × 2.5 m. The nozzle exit is set at $X = 1$ m. The distance from the lunar ground is set as 1 m. The Moon has almost no atmosphere, so the lunar environment is taken as highly vacuum.

### 4.2. Flow field results

The 3D plume field of two 150 N engines is simulated. The lunar ground and the explorer surface are both taken as solid wall boundary. The wall temperature is set as invariably 300 K. The thermal accommodation coefficient is set as 1.0. Fig. 15 is the computation mesh grid of the explorer, the landfall legs and antenna.

Three slices are extracted to display the plume field results, as shown in Fig. 16. The Slice *A* is just between the two 150 N engines and goes through the origin point. The Slice *B* goes through the both axis lines of two engines. The Slice *C* is perpendicular to axis *Y* and goes through the center point of the bottom disk of the landfall leg.

Fig. 17 shows the pressure distribution on the Slice *A*. Fig. 18 shows the static temperature distribution on the Slice *A*. Fig. 19 shows the velocity distribution and streamlines on the Slice *A*.

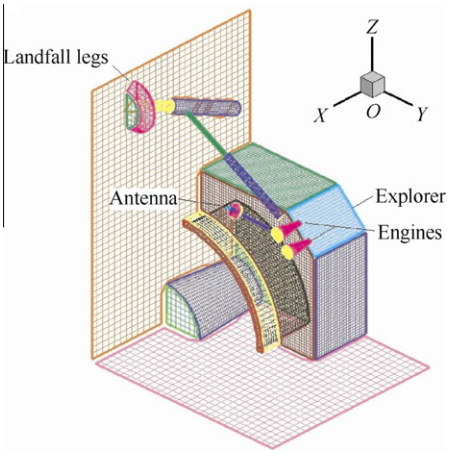


**Fig. 15** Computation mesh grid of the explorer.

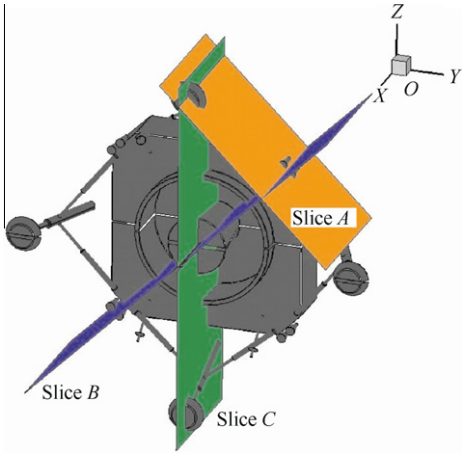


**Fig. 16** Characteristic slices of plume field.

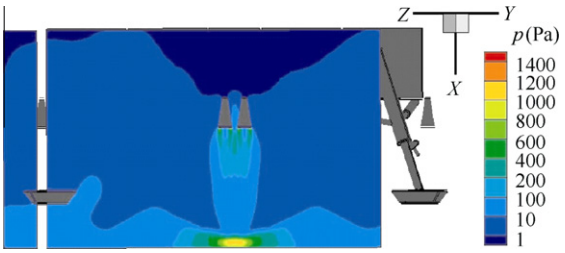


**Fig. 17** Pressure distribution on the Slice *A*.

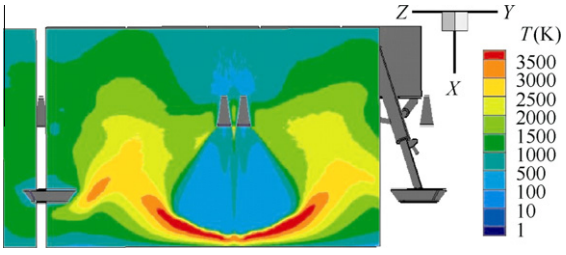


**Fig. 18** Temperature distribution on the Slice *A*.

The flow field of two engines is symmetrical. The nozzle exhaust expands freely at first and finally impacts on the lunar ground. The high-speed gas molecules reflect on the boundary, and are compressed. The maximum density of the plume field on the Slice *B* is 0.002 kg/m$^3$, which appears near the nozzle exit. The maximum pressure, temperature, and velocity of the plume field on the Slice *B* all take place near the lunar ground. Their values are 1400 Pa, 3500 K, and 3000 m/s. The landfall legs also compress the gas flow, which can be clearly seen in Fig. 18.

Fig. 20 shows the pressure distribution on the Slice *B*. Fig. 21 shows the static temperature distribution on the Slice *B*. Fig. 22 shows the velocity distribution and streamlines on the Slice *B*. The maximum pressure of the plume field on the

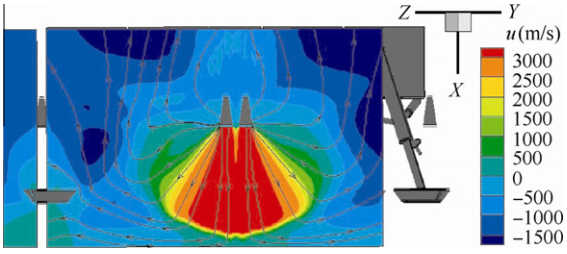


**Fig. 19** Velocity and streamlines on the Slice *A*.

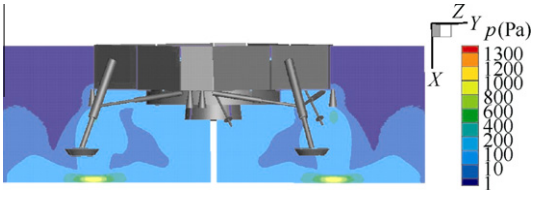


**Fig. 20** Pressure distribution on the Slice *B*.

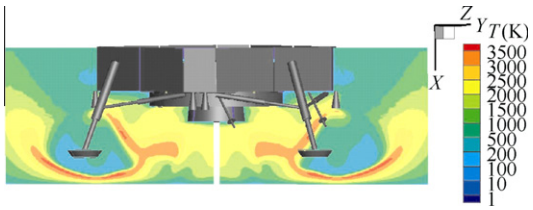


**Fig. 21** Temperature distribution on the Slice *B*.

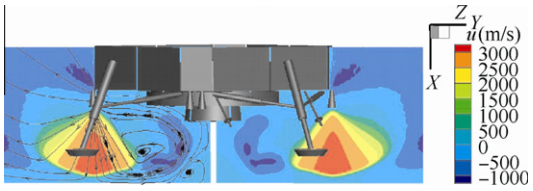


**Fig. 22** Velocity and streamlines on the Slice *B*.

Slice *B* is 1300 Pa, which appears near the lunar ground. The maximum temperature of the plume field on the Slice *B* is 3500 K, which appears near the symmetrical surface of the explorer. The maximum velocity of the plume field on the Slice *B* is 3000 m/s, which appears near the lunar ground.

Fig. 23 shows the pressure distribution on the Slice *C*. Fig. 24 shows the static temperature distribution on the Slice *C*. Fig. 25 shows the Mach number *Ma* distribution and streamlines on the Slice *C*. The gas flow near the Slice *C* mainly comes from the reflection flow on the lunar ground, because it is far from the nozzle exit. So the direction of streamlines goes from the lunar ground.

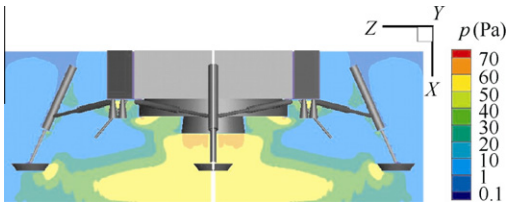


**Fig. 23** Pressure distribution on the Slice *C*.

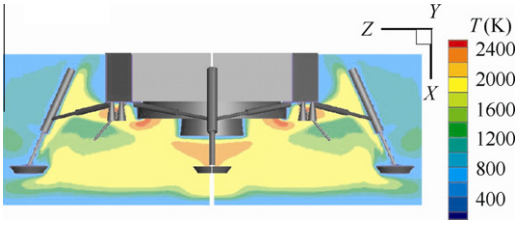


**Fig. 24** Temperature distribution on the Slice *C*.

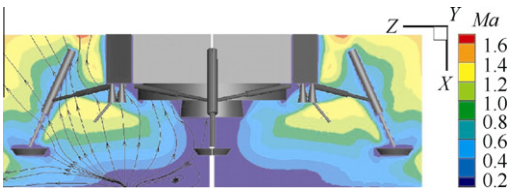


**Fig. 25** Mach number and streamlines on the Slice *C*.

The maximum density and pressure of the plume field on the Slice *C* appear near the explorer bottom. Their values are 0.0003 kg/m$^3$ and 70 Pa. The maximum temperature of the plume field on the Slice *C* is 2400 K. The maximum velocity of the plume field on the Slice *C* is 1800 m/s. The maximum Mach number of the plume field on the Slice *C* is 1.6.

The compression effects of landfall legs can also be observed in the following figures. Because the area of bottom disk is relatively small, its influence is quite limited. The maximum values of gas density, pressure and temperature are respectively 0.00015 kg/m$^3$, 55 Pa and 2000 K.

### *4.3. Plume aerodynamic effects*

The contours of pressure and heat flux at the explorer surface are shown in Figs. 26 and 27. As shown in Fig. 23 of the Slice *C*, the gas pressure near the landfall legs and the protuberant border of explorer bottom is much higher than the surrounding region. As a result on the explorer surface the gas pressure shows the same result. There are four regions at the bottom with higher pressure, which is clearly induced by the existence of four landfall legs. The maximum value of all explorer parts is just on the legs themselves. The heat flux distribution follows the same rules as pressure.

The contours of pressure and heat flux at the explorer bottom are shown in Figs. 28 and 29. Because the landfall legs compress the plume flow, the maximum value of pressure and heat flux appear near the legs. Their values are respectively 40 Pa and 20 000 W/m$^2$.

Fig. 30 shows five characteristic points at the explorer bottom. The pressure and heat flux value are extracted for further comparison and are listed in Table 3.

The pressure and heat flux of points $P_3$ and $P_5$ located near the landfall legs are both about three times of that of $P_1$ and $P_4$. The heat flux of point $P_1$ is smallest because it is located in the backflow region of two engines.

The contours of pressure and heat flux at the landfall legs are shown in Figs. 31 and 32. The maximum value of pressure is about 80 Pa. The maximum value of heat flux is about 45 000 W/m$^2$.

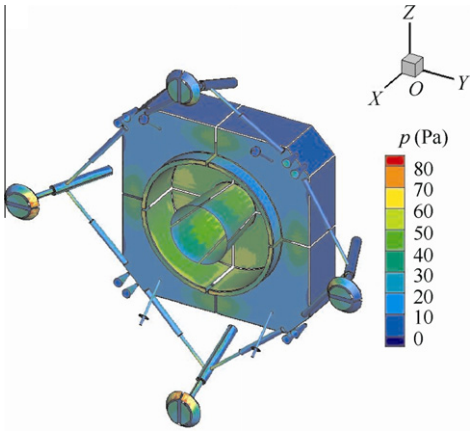


**Fig. 26** Pressure distribution on the explorer surface.

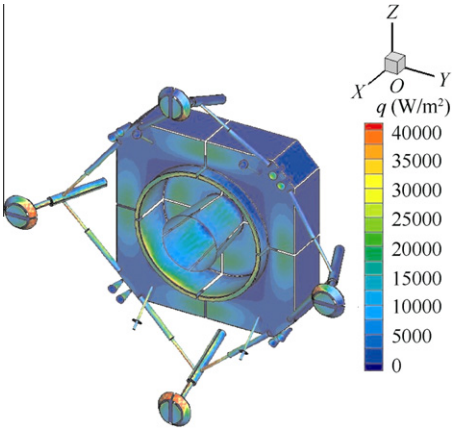


**Fig. 27** Heat flux distribution on the explorer surface.

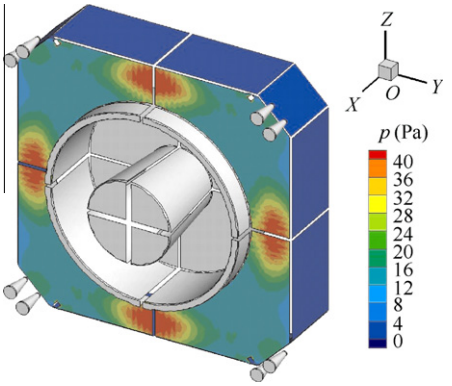


**Fig. 28** Pressure distribution at the explorer bottom.

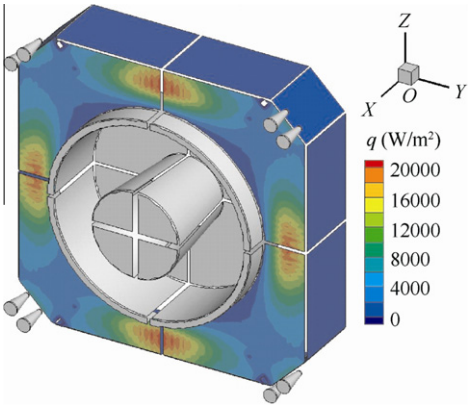


**Fig. 29** Heat flux distribution at the explorer bottom.

The contours of pressure and heat flux at the antenna are shown in Figs. 33 and 34. The maximum value of pressure is about 35 Pa. The maximum value of heat flux is about 35 000 W/m$^2$.

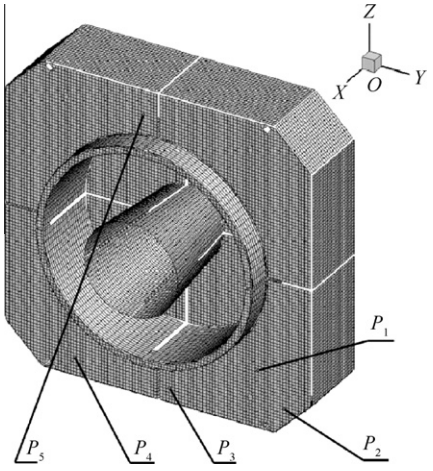


**Fig. 30** Characteristic points at the explorer bottom.

**Table 3** Parameters of characteristic points.

| Points | $X$/m | $Y$/m | $Z$/m | Pressure/Pa | Heat flux/(W·m$^{-2}$) |
|---|---|---|---|---|---|
| $P_1$ | 0.6 | 0.813 | −0.813 | 14.6 | 2684 |
| $P_2$ | 0.6 | 1.025 | −1.025 | 16.75 | 4393 |
| $P_3$ | 0.6 | 0.1 | −1.1 | 45.83 | 19 382 |
| $P_4$ | 0.6 | −0.65 | 1.082 5 | 15.89 | 6225 |
| $P_5$ | 0.6 | 0.1 | 1.1 | 44.30 | 18 728 |

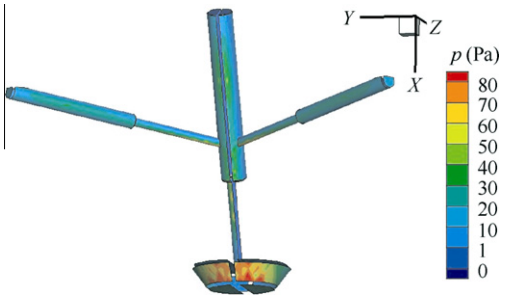


**Fig. 31** Pressure distribution on the landfall legs.

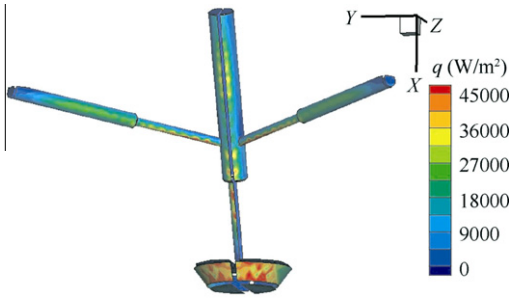


**Fig. 32** Heat flux distribution on the landfall legs.

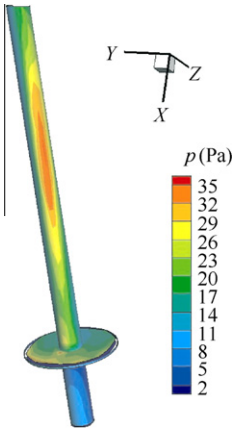


**Fig. 33** Pressure distribution on the antenna.

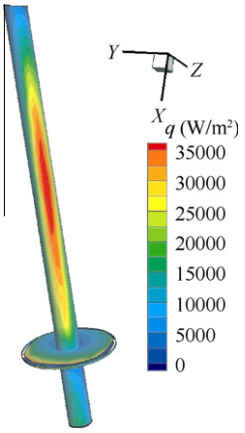


**Fig. 34** Heat flux distribution on the antenna.

## 5. Conclusions

(1) The PWS software based on DSMC method was developed by the research team of Beihang University. The main difference with other mature software is that a decoupling method is utilized to treat the boundary mesh, which has no relation with the computational grids. For the complex structure of the boundary blocks it is more convenient to determine the size of boundary mesh. Test cases are conducted to verify the particle collision and the interaction model of gas molecule and solid surface. The simulation results are compared with the experimental data and the theoretical values, which shows that the computation models are feasible and precise.

(2) The plume aerodynamic effects of two 150 N cushion engines of lunar explorer, which is located at 1 m far from the lunar ground, were numerically simulated by PWS software. The involved components include explorer itself, cushion engines, landfall legs and the antenna, of which the boundary blocks are quite complex. The 3D plume field of two 150 N engines is simulated. Three slices are extracted to display the plume field results. The nozzle exhaust expands freely at first and finally impacts on the lunar ground. The high-speed gas molecules reflect on the boundary, and are compressed. The compression effects of landfall legs can also be observed. There are four regions at the bottom with higher pressure, which is clearly induced by the existence of four landfall legs. The maximum value of all explorer parts is just on the legs themselves. The heat flux distribution follows the same rules as pressure.

## Acknowledgement

This work was supported by the ''Tanyue'' Period Two Research Projects.

## References

1. Bird GA. *Molecular gas dynamics*. Oxford: Clarendon Press; 1976.
2. Wilmoth RG, LeBeau GJ, Carlson AB. DSMC grid methodologies for computing low-density, hypersonic flows about reusable launch vehicles. In: *Proceedings of 31th AIAA thermophysics conference*. New Orleans, USA; 1996.
3. Boyles KA, LeBeau GJ, Lumpkin III FE. The use of virtual subcells in DSMC analysis of orbiter aerodynamics at high altitudes upon reentry. In: *Proceedings of 41th AIAA aerospace sciences meeting and exhibit*. Reno, USA; 2003.
4. LeBeau GJ, Boyles KA, Lumpkin III FE. Virtual sub-cells for the direct simulation Monte Carlo method. In: *Proceedings of 41th AIAA aerospace sciences meeting and exhibit*. Reno, USA; 2003.
5. Ivanov MS, Markelov GN, Gimelshein SF. Statistical simulation of reactive rarefied flows: numerical approach and applications. In: *Proceedings of the 7th AIAA/ASME on joint thermo-physics and heat transfer conference*. Albuquerque, NM, USA; 1998.
6. Alexeenko AA, Gimelshein SF, Levin DA, Gollins RJ. Numerical modeling of axisymmetric and three dimensional flows in MEMS nozzles. In: Proceedings of the 36th AIAA/ASME on joint propulsion conference and exhibt. Huntsville, AL; 2000.
7. Zhong J, Ozawa T, Levinz D.A. Modeling of stardust reentry reacting thermal and chemical ablation flow. AIAA-2007-4551; 2007.
8. Ozawa T, Nompelis I, Levin DA, Barnhardt M, Candler GV. DSMC-CFD comparison of a high altitude, extreme-Mach number reentry flow. In: *Proceedings of the 46th AIAA aerospace sciences meeting and exhibit*. Seattle, Washington, USA; 2008.
9. Ozawa T, Wang A, Levin DA, Modest M. Development of a coupled DSMC-particle photon Monte Carlo method for simulating atomic radiation in hypersonic reentry flows. AIAA-2008-3916; 2008.
10. Gallagher-Rogers AC, Zhong J, Levin DA. Simulation of homogeneous ethanol condensation in nozzle flows using a kinetic method. *J Thermophys Heat Transfer* 2008;**22**(4):695–708.
11. Dietrich S, Boyd ID. A scalar optimized parallel implementation of the DSMC method. In: *32nd AIAA aerospace science meeting and exhibit*. Reno, USA; 1994.
12. Dietrich S, Boyd ID. Parallel implement at ion on the IBM SP-2 of the direct simulation Monte Carlo method. In: *29th AIAA thermophysics conference*. San Diego, USA; 1995.
13. Kannenberg KC, Boyd ID. Three-dimensional Monte Carlo simulations of plume impingement. *J Thermophys Heat Transfer* 1999;**13**(2):226–35.
14. Gimelshein SF, Boyd ID, Ivano MS. Modeling of internal energy transfer in plume flows of polyatomic molecules by the DSMC method. AIAA-99-738; 1999.

15. Boyd ID, Kossi KC, Kannenberg KK, Levin DA, Weaver DP. Modeling the plume contamination and emissions of an ammonia arcjet. AIAA-98-3505; 1998.
16. He BJ, Zhang JH, Cai GB. Numerical simulation of stationary plasma thruster plume. In: *56th International astronautics congress*. Fukuoka, Japan; 2005.
17. Zhang JH, He BJ, Hou FL, Cai GB. Numerical and experimental study of plume impingement effects. In: *57th International astronautics congress*. Valencia, Spain; 2006.
18. Cai GB, He BJ, Zhang JH. Analysis of the thermal effect on satelitte and rocket seperation switch of the SINOSAT-2 satellite orbit transfer engine. In: *58th International astronautics congress*. Hyderabad, India; 2007.
19. Holden M, Wadhams T. Code validation study of laminar shock/boundary layer and shock/shock interactions in hypersonic flow, Part A: experimental measurements. In: *39th AIAA aerospace sciences meeting and exhibit*. Reno, USA; 2001.

**He Bijiao** is a lecturer at School of Astronautics, Beihang University. He received the Ph.D. degree from the same University in 2009. His research interest is the vaccuum plume and control technology.

**Cai Guobiao** is a professor and Ph.D. supervisor at School of Astronautics, Beihang University. He received the PhD degree from the same University in 1996. His research interests include the vacuum plume effects and control technology, the rocket engine optimization and simulation techniques, the rocket engine re-use technology and hybrid rocket engine technology and application.